Applied Surface Science 609 (2023) 155321

Contents lists available at ScienceDirect

Applied Surface Science

journal homepage: www.elsevier.com/locate/apsusc

Full Length Article

Surface-dependent properties and morphological transformations of rutile GeO_2 nanoparticles

José A.S. Laranjeira [a], Sérgio A. Azevedo [a,e], Guilherme S.L. Fabris [b], Anderson R. Albuquerque [c], Mateus M. Ferrer [d], Julio R. Sambrano [a,*]

[a] Modeling and Molecular Simulation Group, São Paulo State University, 17033-360, Bauru, SP, Brazil
[b] Department of Materials Engineering, Federal University of Rio Grande do Norte, 59078-970 Natal, Brazil
[c] Chemistry Institute, Federal University of Rio Grande do Norte, 59078-970 Natal, RN, Brazil
[d] Graduate Program in Materials Science and Engineering, Center for Technology Development, Federal University of Pelotas, 96010-610 Pelotas, RS, Brazil
[e] Federal Institute of Maranhão – IFMA, 65950-000, Barra do Corda, MA, Brazil

ARTICLE INFO

Keywords:
Rutile
Germanium dioxide
Morphology
Wulff
DFT

ABSTRACT

Recently, the knowledge of surface-dependent properties has attracted a lot of attention since it is crucial for materials functionalization based on the morphological control of nanoparticles (NPs). This study describes the surface-dependent properties and morphological transformation routes of rutile germanium dioxide (r-GeO_2) using the density functional theory (DFT) and the Wulff construction procedure. The calculations revealed the following order of relative surface stability: (110) > (100) > (321) > (311) > (201) > (211) > (101) > (103) > (001) > (111), with the Ge-O bonds being attributed to Ge_{4p} –O_{2p} and Ge_{4s} –O_{2p} interactions. The results demonstrate that the different coordination breakages on the outermost polyhedra are related to atomic charges, band gap, relative stability, and Fermi energy. Additionally, a map of the morphological transformation routes and the band alignment were elaborated, showing that cubic, octahedral, or hexadecahedral morphologies can have photocatalytic activity for H_2 production via water splitting. The methodology and results reported herein can help target the synthesis and functionalization of rutile-type materials.

1. Introduction

The class of ultra-wide band gap (UWBG) materials has attracted the attention of researchers and industries due to their potential use as luminescent phosphors, oxygen sensors [1–3], quantum computer components [4], deep-ultraviolet optoelectronic devices [5,6], photosensitive sensors [7], water purifying and food sterilizing agents [8], among others [9]. Furthermore, UWBG materials are promising candidates for high-power and efficient electrical energy conversions [10]. Inside this class of compounds, rutile germanium dioxide (r-GeO_2) has a band gap energy of ~ 4.68 eV and exhibits high transmittance, dielectric constant [11], thermal stability [12], and carrier mobility [13]. On the other hand, it is known that the nanoparticle (NP) morphology depends on synthesis parameters, such as reaction time, temperature, pH, surfactants or the presence of dopants [14,15]. In this regard, Wang et al. [16] synthesized r-GeO_2 NPs with square prism morphologies via the hydrothermal method, which proved to have superior photocatalytic activity compared to the r-TiO_2 for H_2 production by water splitting.

Associations between morphology and nanomaterial features can be made from the knowledge of the structural and electronic properties of its exposed (*hkl*) surfaces. However, a complete description of these properties cannot be easily obtained experimentally. In this sense, computational methods such as electronic structure calculations based on density functional theory (DFT) have been widely used in materials science and engineering [17–20]. The Wulff model [21] allows morphological characterization through the relation between the surface-dependent properties and its relative exposure rate [22]. When combined with theoretical methods, this approach becomes a useful tool to explain or predict experimental results [23–27].

Tamijani et al. [28] showed that the relative stability order of r-GeO_2 surfaces is (110) > (100) > (101) > (001), in agreement with to observed for other rutile-type materials [29–33]. However, these studies are limited to low miller indices surfaces. Especially regarding the r-GeO_2, no studies dealing with the characteristics and routes of morphological transformations of their NPs were found. Furthermore, including non-conventional (*hkl*) indices in surface modeling can open

* Corresponding author.
E-mail address: jr.sambrano@unesp.br (J.R. Sambrano).

https://doi.org/10.1016/j.apsusc.2022.155321
Received 23 August 2022; Received in revised form 11 October 2022; Accepted 13 October 2022
Available online 26 October 2022

new perspectives for experimental studies aiming to obtain them for a specific application.

Motivated by this literature gap, the present research focuses on the structural and electronic study of r-GeO_2 surface-dependent properties based on (DFT) simulations. For this purpose, the (0 0 1), (1 0 0), (1 0 1), (1 0 3), (1 1 0), (1 1 1), (2 0 1), (2 1 1), (3 1 1) and (3 2 1) surfaces were simulated. The results allow the construction of a morphological mapping that can describe all crystalline habits that encompass any surface studied herein. This approach can help experimentalists in the synthesis control to obtain and describe desired NP shapes.

2. Computational setup

The simulations were performed using the DFT methodology implemented in the CRYSTAL17 [34] package in conjunction with the B3LYP-D3 [35], which is the B3LYP functional with the empirical and semi-classical Grimme dispersion correction D3 [36]. The Ge and O atomic centers were described by the 9–7631(511d)G [37] and 6-2111d1G [38] all-electron basis sets, respectively. A modified version of the B3LYP-D3 functional (23.3 % HF exchange) was adopted using the same methodology applied by Gomes et al. [39] to improve its approximation to the experimental reference data [40,41].

In the simulations, the precision of the infinite Coulomb and the HF exchange series was controlled by five parameters α_i, with $i = 1, 2, 3, 4$ and 5, where α_1 is the overlap, α_2 is the penetration for Coulomb integrals, α_3 is the overlap for HF exchange integrals, and α_4 and α_5 are the pseudo-overlaps (HF exchange series). As two-electron contributions are neglected when the overlap between atomic functions is below $10^{-\alpha_i}$, the five parameters α_i were set to 8, 8, 8, 8, and 16, respectively. The convergence criteria were 1.5×10^{-3} Ha $Bohr^{-1}$ for the largest force component, and for electronic energy were set to 10^{-6} hartree/cell. The reciprocal space integration used an 8x8x8 k-point mesh in the irreducible Brillouin zone.

The Hirshfeld-I charge calculation model [42] was used to calculate the atomic charges. This model is a modification of the original Hirshfeld method, where the superposition density of all atoms is replaced by calculating iteratively optimized weighted symmetric functions.

3. Model system

The tetragonal r-GeO_2 structure belongs to the space group *P*4(2)/mnm (n° 136). This structure is formed by [GeO_6] polyhedron and characterized by two lattice parameters ($a = b = 4.3975$Å and $c = 2.959$Å) and the internal parameter $u = 0.3059$ [40], which determines the positions of the O atom with respect to the Ge atom (Fig. 1).

The results of bulk structural optimization using the B3LYP-D3 and B3LYP-D3 (23.3 %) functionals for *a*, *c*, *u* and E_{gap} and the experimental reference data [40,43–45] are shown in Table 1.

The HF modification considerably improved the E_{gap} value from 4.23 eV to 4.68 eV, in agreement with the experimental reference data [45]. This process increased the reliability of predicting the electronic and structural properties of the surfaces. From the optimized bulk structure, it was possible to build symmetrical and stoichiometric 2D slab models (finite in the z-direction but periodic in the x- and y-directions), which were optimized as a function of its internal coordinates.

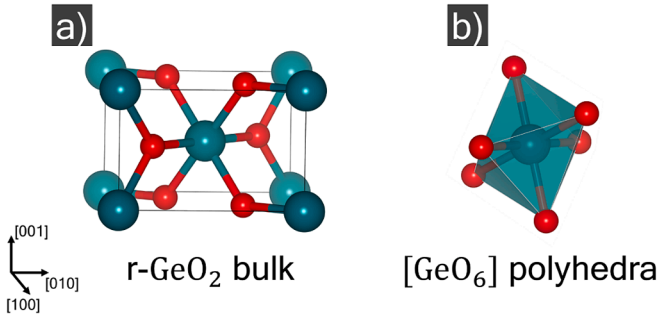

Fig. 1. (a) Unit cell of r-GeO_2 and (b) [GeO_6] polyhedron present in the structure. The green and red spheres represent the Ge and O atoms, respectively.

Table 1
r-GeO_2 lattices parameters (Å) and band gap energy (E_{gap}) (eV).

Functional	$a = b$	c	u	E_{gap}
B3LYP-D3	4.3796 (0.54 %)	2.8992 (0.17 %)	0.3053 (0.21 %)	4.23 (9.62 %)
B3LYP-D3-(23.3 %)	4.3720 (0.72 %)	2.8944 (0.00 %)	0.3052 (0.24 %)	4.68 (0.00 %)
Experimental	–	–	–	4.68 [45]
	4.3975 [40]	2.9590 [40]	0.3059 [40]	–
	4.397 [43]	2.863 [43]	0.3061 [43]	–
	4.397 [44]	2.8619 [44]	0.3060 [44]	–

The values in parentheses are the deviations calculated by the mean of the experimental data.

The number of slab layers (thickness) plays a significant role in the accuracy of surface modeling. The slab thickness was selected as a function of surface energy (E_{surf}) convergence, i.e., when the energy difference between two consecutive slab models is smaller than 0.01 J/m^2. Herein the E_{surf} is defined by: $E_{surf} = (E_{slab} - nE_{bulk})/2A$, where E_{slab} is the total energy of the surface model in the (*hkl*) direction, E_{bulk} is the total energy of the bulk per molecular unit, *n* is the number of molecular units in the model, and *A* is the unit cell area of the slab. The convergence of E_{surf} was reached with slab thicknesses of 32.16, 21.65, 18.48, 13.94, 30.40, 26.72, 17.21, 19.29, 7.73 and 11.31 Å for the (0 0 1), (1 0 0), (1 0 1), (1 0 3), (1 1 0), (1 1 1), (2 0 1), (2 1 1), (3 1 1) and (3 2 1) surfaces, respectively. Fig. 2 shows all surface models and the atomic arrangement of its outermost layers. No reconstruction was observed during the surface simulations.

Taking into account the outermost [GeO_x] polyhedra, the (1 0 0), (1 0 1) and (1 1 0) surfaces have the coordination number (*CN*) equal to 5 (*CN* = 5); the (0 0 1), (2 0 1), (2 1 1), (3 1 1) and (3 2 1), *CN* = 4; and the (1 1 1), *CN* = 3. Furthermore, all surfaces are terminated in two-fold oxygen atoms ($O_{(2f)}$).

The coordination number (*CN*) is used as an approximation to describe the electronic environment in which each atom is inserted. However, using a parameter that counts atoms without distinguishing their distance from a central atom may not accurately describe relatively distorted polyhedra. For example, despite having the same coordination (*CN* = 5), the (1 0 0), (1 1 0), and (1 0 1) surfaces can differ structurally due to distortions from the optimization process (Table 2). Therefore, it is necessary to use the effective coordination number (*ECoN*) [46,47] as a descriptor that quantifies such distortions. In the *ECoN* calculation, bonds are not counted as integers but fractions, with values between 0 and 1 that get closer to zero for larger distances from the central atom. The difference between *CN* and *ECoN* expresses how distorted a polyhedron is.

4. Results and discussion

The $E_{surf}^{non-opt}$ expresses the cutting slab energy, while the E_{surf} incorporates this energy and its variation due to structural optimization (Table 2). The calculated stability order after optimization is (1 1 0) > (1 0 0) > (3 2 1) > (3 1 1) > (2 0 1) > (2 1 1) > (1 0 1) > (1 0 3) > (0 0 1) > (1 1 1). It should be noted that the lower the $E_{surf}(hkl)$, the greater the relative stability of the (*hkl*) surface.

The (1 0 0) and (1 1 0) surfaces are almost degenerate, in agreement with what was observed by Tamijani et al. [28]. The high instability of the (1 1 1) surface can be associated with the lowest coordination of the [GeO_3] polyhedra, which appears only on this surface (Fig. 2).

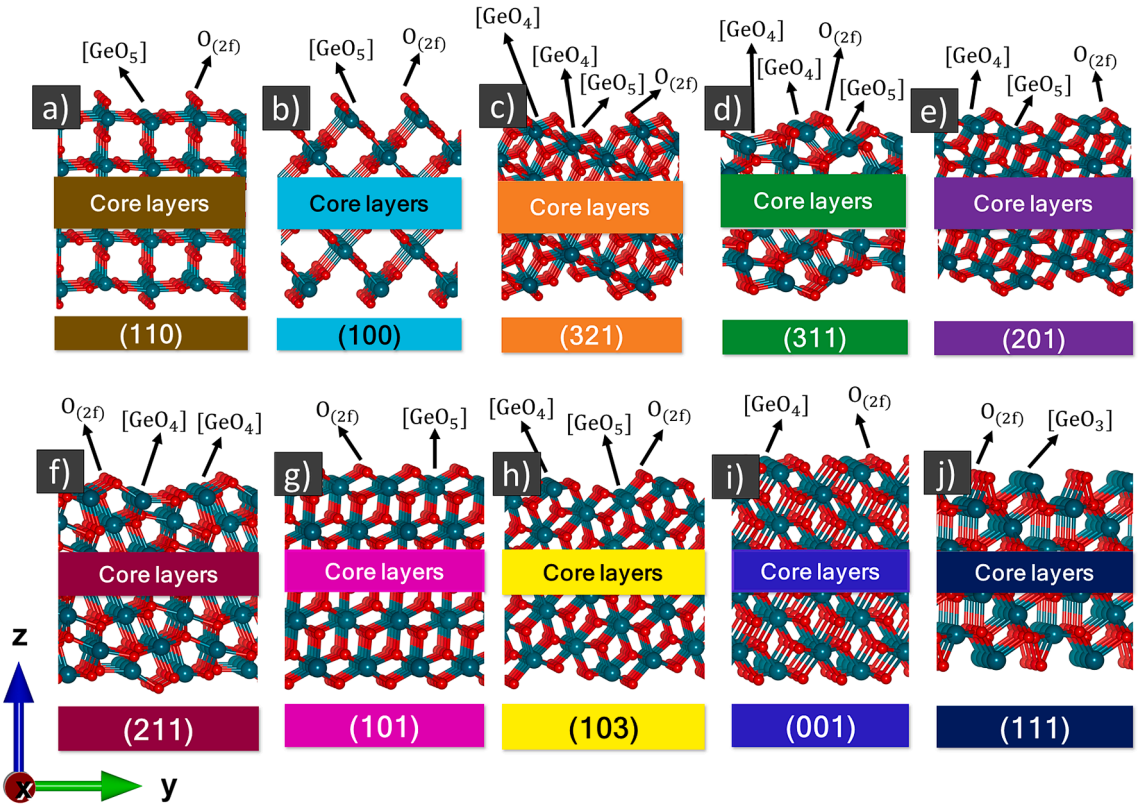

Fig. 2. Side view of the a) (110), b) (100), c) (321), d) (311), e) (201), f) (211), g) (101), h) (103), i) (001) and j) (111) surfaces.

Table 2
Surface energy before ($E_{surf}^{non-opt}$) and after (E_{surf}) structural optimization, band gap energy (E_{gap}) and effective coordination number (*ECoN*) for the outermost [GeO_x] polyhedra with coordination breakdown.

Surface	E_{surf}(J.m^{-2})	$E_{surf}^{non-opt}$(J.m^{-2})	E_{gap}(eV)	*ECoN*
(110)	2.03	12.47	4.05	4.94
(100)	2.04	9.26	4.83	4.76
(321)	2.39	6.64	4.33	3.88
(311)	2.43	5.53	4.21	3.88
(201)	2.45	7.58	4.41	3.97
(211)	2.47	9.48	4.51	3.84
(101)	2.52	9.06	3.82	4.55
(103)	2.88	8.08	3.85	3.96
(001)	3.00	14.50	3.60	3.99
(111)	4.31	12.67	4.16	2.99

As already mentioned, the (110), (101), and (100) surfaces have *CN* = 5. The (110) and (100) are the most stable, probably due to the high values of ECoN (4.94 and 4.76, respectively) when compared to (101) (4.55). On the other hand, the (001), (103), (201), (211), (311) and (321) surfaces possess *CN* = 4.

The (103), (201), (211), (311), and (321) surfaces have more than one polyhedron with coordination breakdown (see Figure S1 in Supplementary Material), which become impossible to associate the *ECoN* or *CN* with their relative stabilities. The (201), (211), (311), and (321) surfaces have the lowest E_{surf} values than the conventional surfaces (101), (001) and (111), and can be more likely to appear in NP morphology. Additionally, these surfaces possess more distorted outermost polyhedra, susceptible to interactions that recover the lost symmetry due to coordination breakdowns.

According to Fig. 3, the smallest differences between $E_{surf}^{non-opt}$ and E_{surf} can be observed for the (201), (321) and (311) surfaces, indicating that these structures were slightly modified in the optimization and

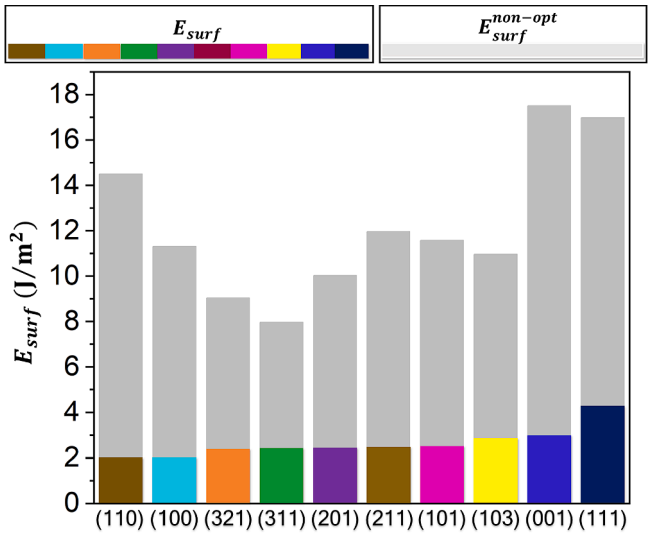

Fig. 3. E_{surf} (J/m^2) (grey) and $E_{surf}^{non-opt}$ (J/m^2) (colorful) before and after optimization, respectively.

could explain their higher stability in comparison with other surfaces that also have *CN* = 4. Considering that these differences may not represent surface stability (being only a tendency), the results demonstrate the importance of considering the optimization effects.

Since dimensionality is crucial for the electronic structure and determines the macroscopic optical properties of NPs, the density of states (DOS) is shown for r-GeO_2 surfaces (Fig. 4). The valence bands (VB) are dominated by states associated with O atoms, while for the conduction bands (CB) the Ge and O contributions are almost equal. Regarding the E_{gap}, it can be noted that the surface with the highest value is the (100),

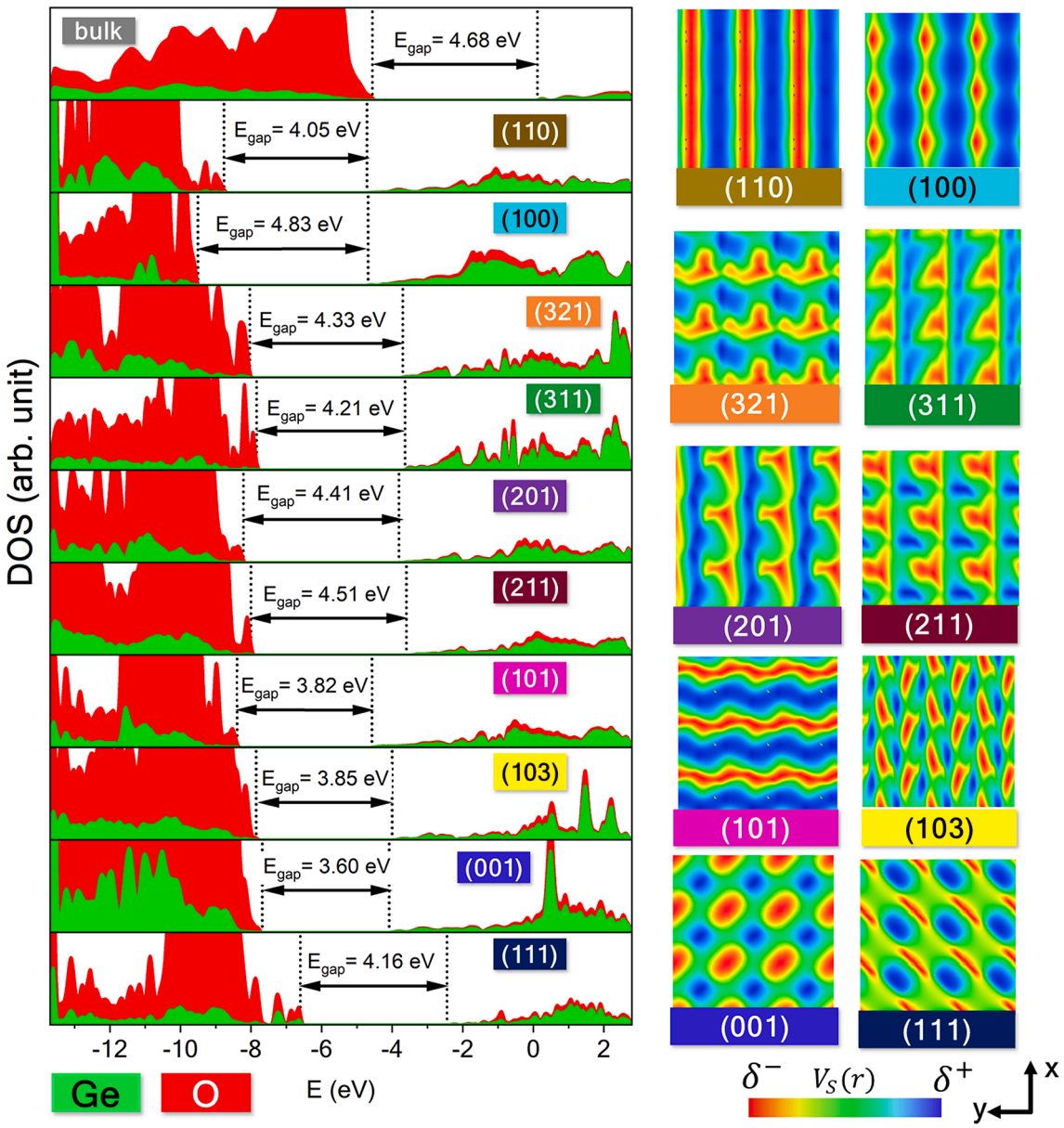

Fig. 4. Projected density of states (DOS) of r-GeO_2 surfaces following the relative stability order (from top to bottom): (110), (100), (321), (311), (201), (211), (101), (103), (001) and (111), and top view (on the right side) of the electrostatic potential surfaces ($V_S(r)$) of each one of them.

i.e., 4.83 eV, in agreement with G. Deng et al. [48], which reported (100) films of r-GeO_2 with E_{gap} = 5.12 eV, value superior to the bulk (4.68 eV). The (001), (101), and (103) surfaces have E_{gap} values below 4.00 eV and are among the most unstable. These differences allow band gap engineering mechanisms to be proposed through the r-GeO_2 morphological control.

Arranging the surfaces to increase the Fermi energy (E_F) (which corresponds to the top of the VB), that is, (100) < (110) < (101) < (201) < (211) < (321) < (311) < (103) < (001) < (111), it can be seen that the surfaces with higher *CN* in their outermost polyhedra are those with lower E_F values, suggesting that the more modified a surface concerning the bulk, the higher its chemical potential.

The electrostatic potential isosurfaces (Fig. 4) show different charge distribution patterns for each surface. For example, there is a pattern of continuous bands of negative charges interspersed with positive charges for the (110), (100), and (101) surfaces. The (100) and (110) surfaces show wider bands of positive charge density. The (001), (103), (111), (201), (211), (311), and (321) surfaces exhibit more significant areas associated with charge neutrality (in green), evidencing that NPs with these exposed surfaces generally have a greater tendency to exhibit long-distance interactions.

Fig. 5 shows the analysis results performed using the Crystal Orbital Hamilton Population (COHP) [49] method for the Ge – O bonds on each surface. Table S1 (more details in Supplementary Information) includes the different contributions of the orbital pairs and the corresponding energies observed from curve integration for the intervals considered (ICOHP). On all surfaces, only anti-bonding interactions occur in the CB, and in the VB has a predominance of bonding interactions. Furthermore, it can be verified that the (001), (101), and (103) surfaces exhibit lower ICOHP values, suggesting more intense Ge-O bonds in the coordination polyhedra on these surfaces.

The Ge_{3d} –O_{2s} and Ge_{3d} –O_{2p} interactions were not considered, as they did not exhibit significant values of ICOHP. The Ge – O bonds are interactions predominantly of the Ge_{4p} –O_{2p} and Ge_{4s} –O_{2p} type, indicating the occurrence of hybridization between s and p orbitals of the Ge atom. The Ge_{4p} –O_{2s} and Ge_{4s} –O_{2s} orbital interactions result in anti-

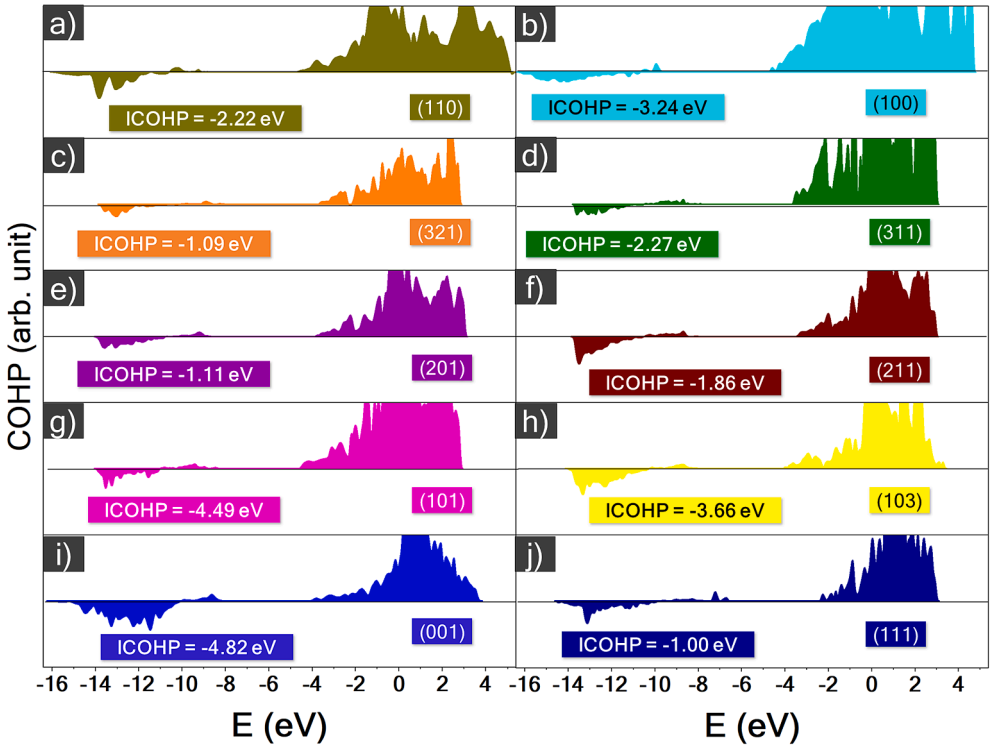

Fig. 5. Crystal Orbital Hamilton Population (COHP) for the Ge – O bonds on the (0 0 1), (1 0 0), (1 0 1), (1 0 3), (1 1 0), (1 1 1), (2 0 1), (2 1 1), (3 1 1) and (3 2 1) r-GeO_2 surfaces and ICOHP (eV) values calculated up to Fermi level. The positive and negative values correspond to anti-bonding and bonding states, respectively.

bonding orbitals, with the $Ge_{4p} - O_{2s}$ being responsible for the most significant number of anti-bonding states.

Table S2 (more details in Supplementary Information) shows the Hirshfeld atomic charges of the outermost polyhedra. For comparison, in the r-GeO_2 bulk, the O atom has a charge of −1.159, while on the (1 1 1) surface, this value is −0.460. The (1 1 0), (0 0 1), (1 0 1), and (1 0 0) surfaces are those with the greatest charge module values for the total charge average of the O atom. These surfaces also have higher ECoN values, demonstrating that the charge of O atoms is associated with polyhedra distortions: the greater the distortions, the higher the charges of the O atoms.

The total charge associated with Ge atoms varies between +2.254 for the (1 1 0) surface and +1.039 for the (1 1 1). Except for the (1 1 1) surface (which has a lower charge on the outermost Ge atoms due to its low coordination), the charges of each central Ge atom are always greater than +2.000. Regarding the average charge of the outermost $[GeO_n]$ polyhedra ($Q_{polyhedra} = (n.Q_O + Q_{Ge})/(n+1)$), the highest charges can be seen for the (1 0 0), (1 1 0), and (1 0 1) surfaces. In addition, these surfaces exhibit greater $Q_{polyhedra}$ values, as demonstrated in Fig. 4, in which it is possible to observe that these surfaces also have greater charge density (areas in red or blue).

In the r-GeO_2 bulk, the charges of Ge atoms are higher due to the absence of bond breakages. In contrast, the charges were redistributed due to O vacancies in the outermost atomic layers of the surfaces. Moreover, the charge modules tend to increase in the innermost layers of the surface models, considering that they reproduce the bulk structure.

Using the Wulff model together with the $E_{surf}^{non-opt}$ and E_{surf} values (see Table 1), it was possible to represent the crystals referring to these two states. As it can be seen, in the crystal obtained from the $E_{surf}^{non-opt}$, only the (3 1 1) and (1 0 3) surfaces become exposed, with a relative exposure rate of 92.8 % and 7.2 %, respectively (see Fig. 6).

As a result of optimization, the (1 1 0), (1 0 0), (3 2 1), (1 0 1), (2 0 1), (2 1 1) and (3 1 1) become exposed. The (1 0 0) and (1 1 0) surfaces are the most stable and almost degenerate for E_{surf} values exhibit very close relative exposure rates, i.e., 22.2 % and 22.7 %, respectively. The exposure of each surface is not strictly related to its E_{surf}, since the (1 0 1) plane has greater E_{surf} than the (1 0 0) and (1 1 0) surfaces and a relative exposure of 24.1 %. This occurs because of the different growth dynamics of each plane, where different variations in the relative exposure rate are observed for the same variations of E_{surf}. If the (1 0 1) surface had E_{surf} close to that of the (1 0 0) and (1 1 0) surfaces, the NPs would look similar to v_7 (Fig. 7).

According to the model used by Laranjeira et al. [51,52], it is possible to impose the modulation of the E_{surf} value for each surface to obtain a crystal corresponding to the highest possible exposure for each (*hkl*) surface ($v_1 - v_{10}$), which is represented by the ratio of surface energies (Γ) matrix, where all E_{surf} values were divided by the E_{surf} value of the most stable surface (in this case, the $E_{surf}^{(110)}$).

In Fig. 7, the crystals e_{1-10} correspond to the combinations of E_{surf} modulations occurred in v_{1-10}. For example, in crystal e_1 the E_{surf} are simultaneously changed for the (1 1 0) and (1 0 0) surfaces, as occurred in v_1 and v_2, respectively. As the Γ^* decreases, the characteristic morphology of each (*hkl*) surface becomes evident, as are the cases of $\Gamma_{(110)}$ and $\Gamma_{(100)}$. According to the graph, the morphologies are rod-like. The morphologies obtained by decreasing $\Gamma_{(201)}$,$\Gamma_{(101)}$ and $\Gamma_{(111)}$, exhibit an octahedral shape, while those associated with decreases in $\Gamma_{(321)}$, $\Gamma_{(311)}$ and $\Gamma_{(211)}$ have hexadecahedral geometric shapes. For the $\Gamma_{(001)}$ and $\Gamma_{(111)}$, the crystals become increasingly flattened. As a consequence, when Γ^* is closer to zero, the lateral facets practically disappear, forming disk-like morphologies.

Considering that the surfaces with the corner of the coordination polyhedra exposed have the biggest growth rate compared to those with the face exposed [53], C. Jing et al. [54] proposed the velocity surface growth order: (1 1 1) > (0 0 1) > (1 0 1) > (1 0 0) > (1 1 0) for r-GeO_2. This order agrees with the stability order calculated here; most stable surfaces have the lowest velocity growth. The authors also described a growth mechanism for rod-like r-GeO_2 nanoparticles (Fig. 8a and 8b). Take into account that the surfaces with lower E_{surf} have preferential

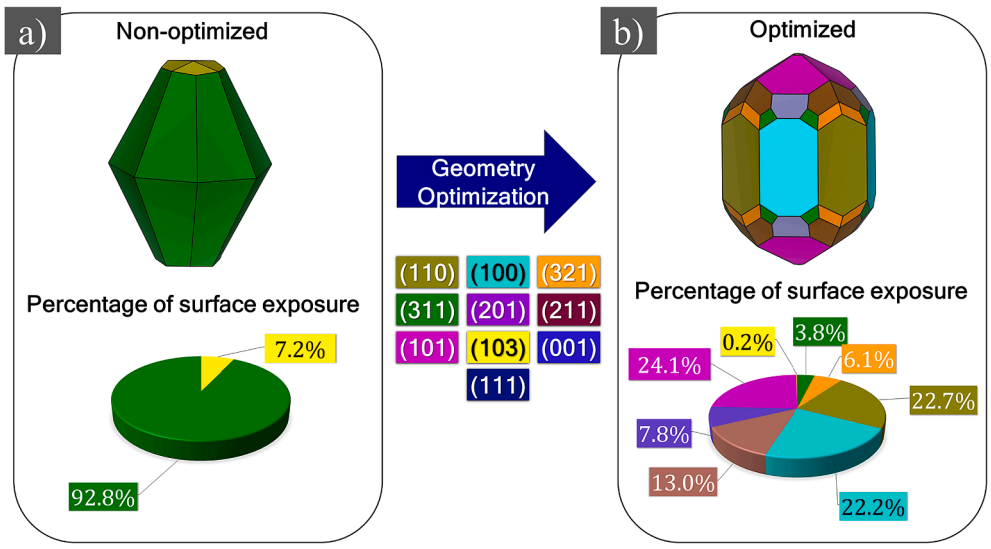

Fig. 6. Morphology obtained from (a) $E_{surf}^{non-opt}$ and (b) E_{surf} values [50] and the respective percentages of exposed surface area.

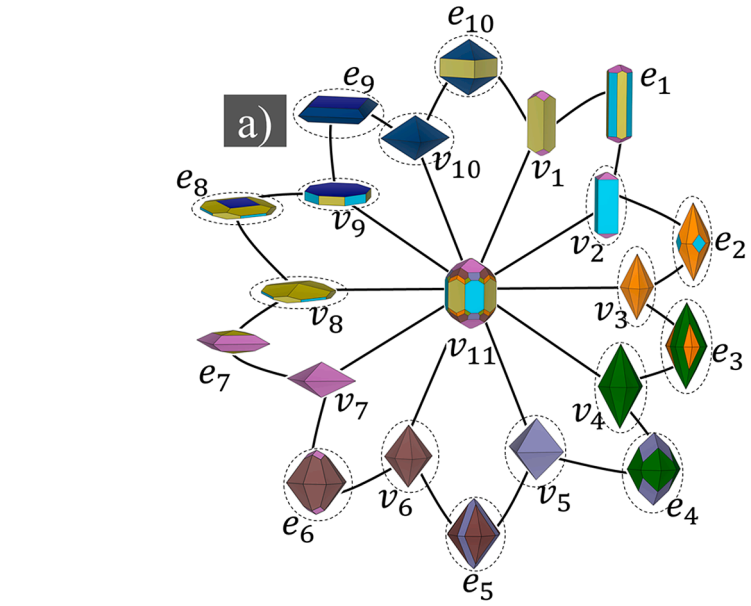

b) Surface Energy Ratio ($\Gamma_{(hkl)} = E_{surf\ (hkl)}/E_{surf\ (110)}$)

	v_1	v_2	v_3	v_4	v_5	v_6	v_7	v_8	v_9	v_{10}	v_{11}
(110)	0.44	1.00	1.00	1.00	1.00	1.00	1.00	1.00	1.00	1.00	1.00
(100)	1.01	0.44	1.01	1.01	1.01	1.01	1.01	1.01	1.01	1.01	1.01
(321)	1.18	1.18	0.44	1.18	1.18	1.18	1.18	1.18	1.18	1.18	1.18
(311)	1.20	1.20	1.20	0.44	1.20	1.20	1.20	1.20	1.20	1.20	1.20
(201)	1.21	1.21	1.21	1.21	0.44	1.21	1.21	1.21	1.21	1.21	1.21
(211)	1.22	1.22	1.22	1.22	1.22	0.44	1.22	1.22	1.22	1.22	1.22
(101)	1.24	1.24	1.24	1.24	1.24	1.24	0.35	1.24	1.24	1.24	1.24
(103)	1.42	1.42	1.42	1.42	1.42	1.42	1.42	0.25	1.42	1.42	1.42
(001)	1.48	1.48	1.48	1.48	1.48	1.48	1.48	1.48	0.15	1.48	1.48
(111)	2.13	2.13	2.13	2.13	2.13	2.13	2.13	2.13	2.13	0.44	2.13

Fig. 7. (a) Graph of morphologies with all possible variations for surfaces with maximum exposed areas and combined two by two, highlighting morphologies with exposed surfaces with possible photocatalytic activity for H_2 production via water splitting, and (b) matrix modification of the represented morphologies in (a).

growth in NPs, here was proposed a new growth mechanism for rod-like r-GeO_2 (Fig. 8c), where the sharps that before were associated with (1 1 1) surface growth can be due to (3 2 1).

Wang et al. [16] compared the r-GeO_2 and r-TiO_2 based on their photocatalytic activities for H_2 production via water splitting. These authors synthesized r-GeO_2 by the hydrothermal method and obtained a

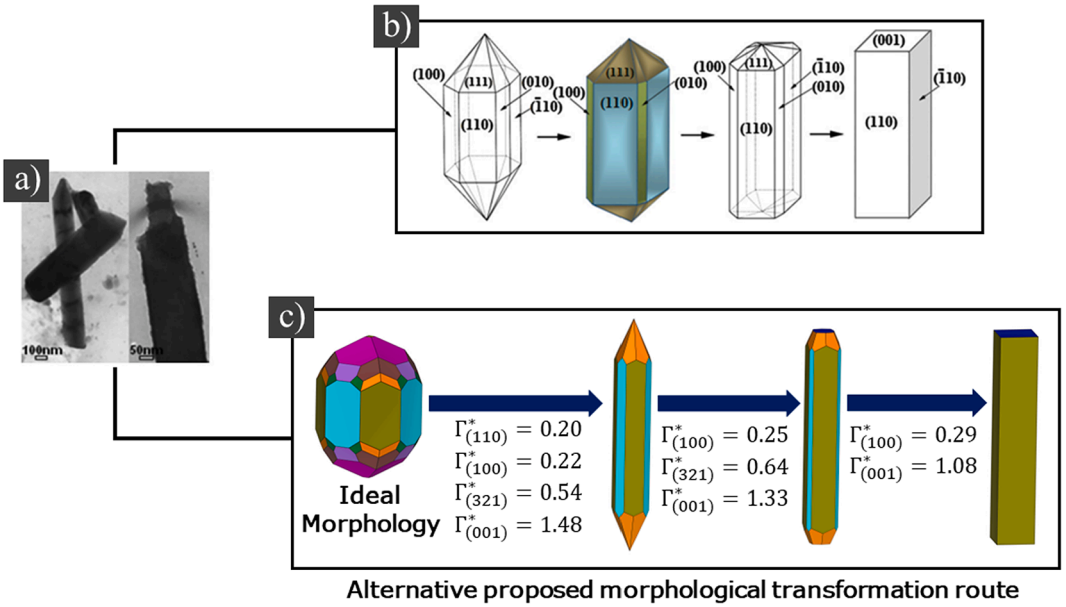

Fig. 8. (a) Transmission Electron Microscopy (TEM) images of rod-like r-GeO_2 obtained via liquidus phase deposition for 0.5–2 h, (b) proposed morphological transformation route by C. Jing et al. [54] and (c) alternative route using the results reported here.

square prism morphology (Fig. 10c). From TEM data, it can be verified that one of the exposed surfaces in the crystal is the (1 1 0). However, according to the band alignment (Fig. 9), the (1 1 0) surface does not have photocatalytic activity for the H^+/H_2 process. This suggests the occurrence of another exposed surface, the (0 0 1). Through modulations in $\Gamma_{(001)}$ and $\Gamma_{(110)}$ (Fig. 9a and 9b), it is possible to obtain the theoretical morphology corresponding to experimentally observed NP.

Furthermore, the (0 0 1), (1 0 3), (2 0 1), (2 1 1), (3 1 1) and (3 2 1) surfaces have a band alignment favorable for the production of H_2 (Fig. 9). Nonetheless, this does not mean that under experimental conditions, it would be possible to produce H_2 in the same way for all mentioned surfaces since factors such as the kinetics of different reactions for each surface must be considered. The surfaces with $CN = 5$ in their outermost polyhedra do not have a conduction band minimum

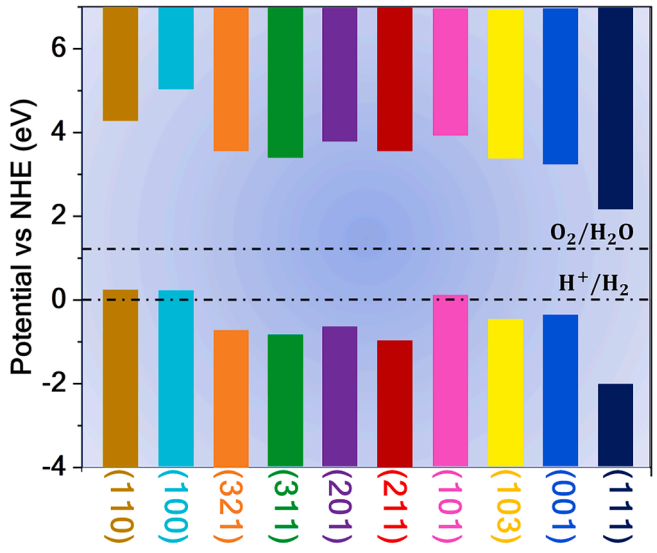

Fig. 9. Band alignment for r-GeO_2 surfaces, based on the methodology reported by Toroker et al. [55]. The positions of the conduction band minimum (E_{CBM}) and the valence band maximum (E_{VBM}) are defined by $E_{CBM/VBM} = E_{BGC} \pm 0.5E_{gap} - E_e$, where E_{BGC} is the energy of the band gap center, and E_e is the Normal Hydrogen Electrode (NHE) potential (4.44 eV).

favorable for the occurrence of the H^+/H_2 process.

In addition to the (0 0 1) surface, it is observed that the NPs with (1 1 1), (2 0 1), (2 1 1), (3 1 1), and (3 2 1) exposed facets tend to have photocatalytic activity for H_2 production. In short, cubic, octahedral or hexadecahedral morphologies have possible photocatalytic activity for r-GeO_2-based systems (Fig. 10).

5. Conclusions

The relative surface stability order (1 1 0) > (1 0 0) > (3 2 1) > (3 1 1) > (2 0 1) > (2 1 1) > (1 0 1) > (1 0 3) > (0 0 1) > (1 1 1) was determined for r-GeO_2. The (2 1 1), (2 0 1) and (3 2 1) surfaces occupy the middle part of the stability order and exhibit chemical and structural characteristics of interest with low *ECoN* values in the outermost polyhedra, demonstrating the importance of considering surfaces with (*hkl*) indices higher than the low Miller indices. The COHP analysis showed that the (0 0 1), (1 0 1) and (1 0 3) surfaces exhibit a greater number of bonding interactions, indicating that the Ge – O bonds present in the coordination polyhedra on these surfaces are more intense and that the $Ge_{4p} - O_{2p}$ and $Ge_{4s} - O_{2p}$ couplings are responsible for bond stabilization in all analyzed systems.

It was also demonstrated that the (0 0 1) surface possesses the lowest E_{gap} value (3.60 eV), while the (1 0 0) surface has the highest (4.83 eV), evidencing that the optoelectronic properties of r-GeO_2-systems can be significantly altered according to morphology. Based on the E_{surf} values and the Wulff construction, it was possible to make a systematically morphological transformation mapping and to know the characteristic morphology of each (*hkl*) surface. This approach allows a better understanding of the relationship between the NP morphology and the material properties, as exemplified in the determination of morphologies with photocatalytic activity for H_2 production via water splitting.

CRediT authorship contribution statement

José A.S. Laranjeira: Conceptualization, Methodology, Software, Validation, Formal analysis, Investigation, Writing – original draft, Writing – review & editing. **Sérgio A. Azevedo:** Data curation, Validation, Investigation, Writing – review & editing. **Guilherme S.L. Fabris:** Data curation, Validation, Investigation, Visualization. **Anderson R. Albuquerque:** Methodology, Validation, Data curation, Visualization,

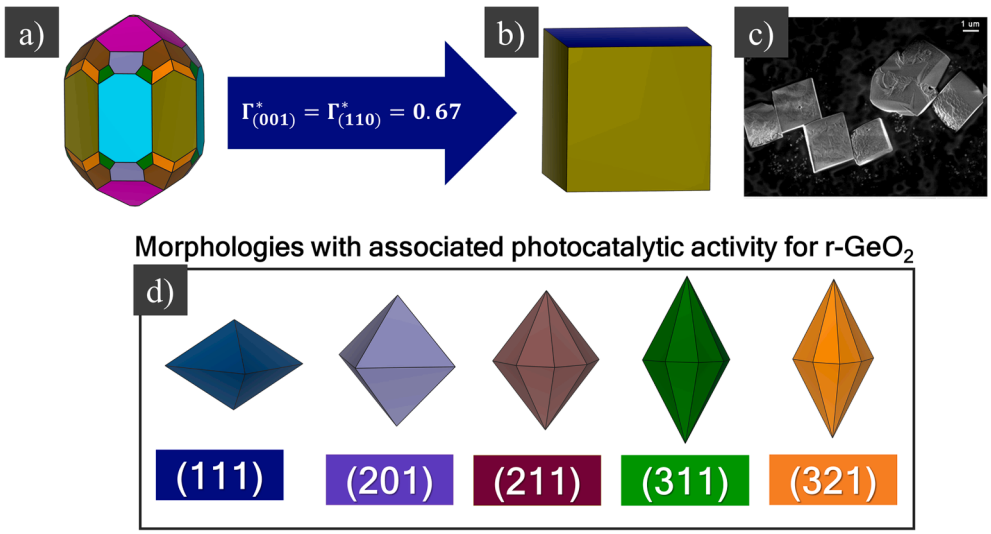

Fig. 10. (a) Ideal crystal, (b) square prisms of the theoretical r-GeO_2, (c) experimental crystal synthesized by Wang et al. via the hydrothermal method [16] and (d) morphologies with associated photocatalytic activity. Reprinted with permission of ref [16].

Writing – review & editing. **Mateus M. Ferrer:** Data curation, Validation, Visualization. **Julio R. Sambrano:** Conceptualization, Validation, Visualization, Supervision, Project administration, Funding acquisition, Writing – original draft, Writing – review & editing.

Declaration of Competing Interest

The authors declare that they have no known competing financial interests or personal relationships that could have appeared to influence the work reported in this paper.

Data availability

Data will be made available on request.

Appendix A. Supplementary material

Supplementary data to this article can be found online at https://doi.org/10.1016/j.apsusc.2022.155321.

References

[1] L. Nagarajan, R.A. de Souza, D. Samuelis, I. Valov, A. Börger, J. Janek, K.D. Becker, P.C. Schmidt, M. Martin, A chemically driven insulator–metal transition in non-stoichiometric and amorphous gallium oxide, Nature Materials 2008 7:5. 7 (2008) 391–398. 10.1038/nmat2164.
[2] J. Kim, T. Sekiya, N. Miyokawa, N. Watanabe, K. Kimoto, K. Ide, Y. Toda, S. Ueda, N. Ohashi, H. Hiramatsu, H. Hosono, T. Kamiya, Conversion of an ultra-wide bandgap amorphous oxide insulator to a semiconductor, NPG Asia Materials 2017 9:3. 9 (2017) e359–e359. 10.1038/am.2017.20.
[3] E. Chikoidze, D.J. Rogers, F.H. Teherani, C. Rubio, G. Sauthier, H.J. von Bardeleben, T. Tchelidze, C. Ton-That, A. Fellous, P. Bove, E. v. Sandana, Y. Dumont, A. Perez-Tomas, Puzzling robust 2D metallic conductivity in undoped β-Ga2O3 thin films, Materials Today Physics. 8 (2019) 10–17. 10.1016/J.MTPHYS.2018.11.006.
[4] J. He, Comparison between The ultra-wide band gap semiconductor AlGaN and GaN, IOP Conf. Ser Mater. Sci. Eng. 738 (2020), 012009, https://doi.org/10.1088/1757-899X/738/1/012009.
[5] E. Chikoidze, C. Sartel, I. Madaci, H. Mohamed, C. Vilar, B. Ballesteros, F. Belarre, E. del Corro, P. Vales-Castro, G. Sauthier, L. Li, M. Jennings, V. Sallet, Y. Dumont, A. Pérez-Tomás, P-Type Ultrawide-Band-Gap Spinel ZnGa2O4: new perspectives for energy electronics, Cryst. Growth Des. 20 (2020) 2535–2546, https://doi.org/10.1021/ACS.CGD.9B01669/ASSET/IMAGES/ACS.CGD.9B01669.SOCIAL.JPEG_V03.
[6] I. Hany, G. Yang, C.C. Chung, Fast X-ray detectors based on bulk β-Ga2O3 (Fe), J. Mater. Sci. 55 (2020) 9461–9469, https://doi.org/10.1007/S10853-020-04665-9/TABLES/1.
[7] C. v. Ramana, G. Carbajal-Franco, R.S. Vemuri, I.B. Troitskaia, S.A. Gromilov, V. v. Atuchin, Optical properties and thermal stability of germanium oxide (GeO2) nanocrystals with α-quartz structure, Materials Science and Engineering: B. 174 (2010) 279–284. 10.1016/J.MSEB.2010.03.060.
[8] K.A. Mengle, S. Chae, E. Kioupakis, Quasiparticle band structure and optical properties of rutile GeO2, an ultra-wide-band-gap semiconductor, J. Appl. Phys. 126 (2019), 085703, https://doi.org/10.1063/1.5111318.
[9] M. Higashiwaki, R. Kaplar, J. Pernot, H. Zhao, Ultrawide bandgap semiconductors, Appl. Phys. Lett. 118 (2021), 200401, https://doi.org/10.1063/5.0055292.
[10] S. Chae, K. Mengle, K. Bushick, J. Lee, N. Sanders, Z. Deng, Z. Mi, P.F.P. Poudeu, H. Paik, J.T. Heron, E. Kioupakis, Toward the predictive discovery of ambipolarly dopable ultra-wide-band-gap semiconductors: the case of rutile GeO2, Appl. Phys. Lett. 118 (2021), 260501, https://doi.org/10.1063/5.0056674.
[11] H. Takane, K. Kaneko, Establishment of a growth route of crystallized rutile GeO2 thin film (≧1 μm/h) and its structural properties, Appl. Phys. Lett. 119 (2021), 062104, https://doi.org/10.1063/5.0060785.
[12] S. Chae, K.A. Mengle, R. Lu, A. Olvera, N. Sanders, J. Lee, P.F.P. Poudeu, J. T. Heron, E. Kioupakis, Thermal conductivity of rutile germanium dioxide, Appl. Phys. Lett. 117 (2020), 102106, https://doi.org/10.1063/5.0011358.
[13] K. Bushick, K.A. Mengle, S. Chae, E. Kioupakis, Electron and hole mobility of rutile GeO2 from first principles: an ultrawide-bandgap semiconductor for power electronics, Appl Phys Lett. 117 (2020), 182104, https://doi.org/10.1063/5.0033284.
[14] P. Chen, J. Liu, B. Yang, M. Gao, L. You, Y. Zhang, Z. Li, L. Guo, T. Li, M. Liu, Facile synthesis of new polyhedron-like WO 3 /butterfly-like Ag 2 MoO 4 p–n junction photocatalysts with higher photocatalytic activity in UV/solar region light, New J. Chem. 44 (2020) 3194–3205, https://doi.org/10.1039/C9NJ05801J.
[15] T. Cheng, H. Gao, X. Sun, T. Xian, S. Wang, Z. Yi, G. Liu, X. Wang, H. Yang, An excellent Z-scheme Ag2MoO4/Bi4Ti3O12 heterojunction photocatalyst: construction strategy and application in environmental purification, Adv. Powder Technol. 32 (2021) 951–962, https://doi.org/10.1016/J.APT.2021.01.039.
[16] R. Wang, Q. Li, W. Li, P. Jiang, R. Cong, T. Yang, d10 or d0? Theoretical and experimental comparison between rutile GeO2 and TiO2 for photocatalytic water splitting, Chem. Commun. 57 (2021) 536–539, https://doi.org/10.1039/D0CC06883G.
[17] M. Rostami, M. Afkani, M.R. Torkamani, F. Kanjouri, Bulk and surface DFT investigations of the electronic and magnetic properties of CsXNO (X = Mg, Ca and Sr) quaternary Heusler alloys, Mater. Chem. Phys. 248 (2020), 122923, https://doi.org/10.1016/J.MATCHEMPHYS.2020.122923.
[18] B. Wei, M. Calatayud, The subsurface diffusion of hydrogen on rutile TiO2 Surfaces: a Periodic DFT Study, Top Catal. 65 (2022) 270–280, https://doi.org/10.1007/S11244-021-01518-W/FIGURES/8.
[19] T. Zhang, X. Yang, Q. Ge, CH4 dissociation and CC coupling on Mo-terminated MoC surfaces: a DFT study, Catal. Today. 339 (2020) 54–61, https://doi.org/10.1016/J.CATTOD.2019.03.020.
[20] R. Oukhrib, B. el Ibrahimi, H. Abou Oualid, Y. Abdellaoui, S. el Issami, L. Bazzi, M. Hilali, H. Bourzi, In silico investigations of alginate biopolymer on the Fe (110), Cu (111), Al (111) and Sn (001) surfaces in acidic media: quantum chemical and molecular mechanic calculations, J Mol Liq. 312 (2020), 113479, https://doi.org/10.1016/J.MOLLIQ.2020.113479.
[21] G. Wulff, Xxv. Zur, Frage der Geschwindigkeit des Wachsthums und der Auflösung der Krystallflächen, Z Kristallogr Cryst. Mater. 34 (1901), https://doi.org/10.1524/zkri.1901.34.1.449.
[22] A.R. Albuquerque, I.M.G. Santos, J.R. Sambrano, Propriedades estruturais e eletrônicas de nanofilmes de TiO2 anatase: cálculos B3LYP-D* em sistemas periódicos bidimensionais, Quim Nova. 37 (2014) 1318–1323, https://doi.org/10.5935/0100-4042.20140187.

[23] V. Teodoro, A.F. Gouveia, T.R. Machado, A.B. Trench, N. Jacomaci, M. Assis, G. E. Marques, M.D. Teodoro, M.A. San-Miguel, J. Andrés, J. Bettini, E. Longo, Connecting morphology and photoluminescence emissions in β-Ag2MoO4 microcrystals, Ceram Int. 48 (2022) 3740–3750, https://doi.org/10.1016/J.CERAMINT.2021.10.156.
[24] L.H. da S. Lacerda, M.A. San-Miguel, DFT approaches unraveling the surface and morphological properties of MnMoO4, Appl Surf Sci. 567 (2021) 150882. 10.1016/J.APSUSC.2021.150882.
[25] A. Piovano, M. D'Amore, T. Wada, P. Cleto Bruzzese, G. Takasao, A. Thakur, P. Chammingkwan, M. Terano, B. Civalleri, S. Bordiga, T. Taniike, E. Groppo, Revisiting the identity of δ-MgCl2: Part II. Morphology and exposed surfaces studied by vibrational spectroscopies and DFT calculation, J Catal. 387 (2020) 1–11, https://doi.org/10.1016/J.JCAT.2020.04.017.
[26] L. Cheng, X. Yu, J. Zhang, W. Li, C. Zhao, Z. Wang, L. Jin, DFT investigations into surface stability and morphology of δ-MoC catalyst, Appl. Surf. Sci. 497 (2019), 143790, https://doi.org/10.1016/J.APSUSC.2019.143790.
[27] X. Tian, P. Li, T. Wang, Morphology of MoP catalyst under hydrogenation conditions: a DFT based thermodynamics study, Molecular, Catalysis. 464 (2019) 57–62, https://doi.org/10.1016/J.MCAT.2018.12.010.
[28] A. Abbaspour Tamijani, E. Ebrahimiaqda, Anomalous behavior of rutile GeO2 facets: A computational study, Mater Chem Phys. 199 (2017) 552–556. 10.1016/J.MATCHEMPHYS.2017.07.027.
[29] D.A. Tompsett, S.C. Parker, M.S. Islam, Rutile (β-)MnO2 surfaces and vacancy formation for high electrochemical and catalytic performance, J. Am. Chem. Soc. 136 (2014) 1418–1426, https://doi.org/10.1021/JA4092962/SUPPL_FILE/JA4092962_SI_001.PDF.
[30] M. de Aquino Barbosa, G. da Silva Lopes, M.M. Fabris, D.H.M. de Ferrer, J.R. S. Azevedo, Computational simulations of morphological transformations by surface structures: the case of rutile TiO_2 phase, Mater. Res. 20 (2017) 920–925, https://doi.org/10.1590/1980-5373-MR-2016-0709.
[31] F. Jiang, L. Yang, D. Zhou, G. He, J. Zhou, F. Wang, Z.G. Chen, First-principles atomistic Wulff constructions for an equilibrium rutile TiO2 shape modeling, Appl. Surf. Sci. 436 (2018) 989–994, https://doi.org/10.1016/J.APSUSC.2017.12.050.
[32] T.A. Mellan, R. Grau-Crespo, Density functional theory study of rutile VO2 surfaces, J. Chem. Phys. 137 (2012), 154706, https://doi.org/10.1063/1.4758319.
[33] A. Beltrán, J. Andrés, J.R. Sambrano, E. Longo, Density functional theory study on the structural and electronic properties of low index rutile surfaces for TiO2/SnO2/TiO 2 and SnO2/TiO2/SnO2 composite systems, J. Phys. Chem. A 112 (2008) 8943–8952, https://doi.org/10.1021/JP801604N/ASSET/IMAGES/LARGE/JP-2008-01604N_0003.JPEG.
[34] R. Dovesi, A. Erba, R. Orlando, C.M. Zicovich-Wilson, B. Civalleri, L. Maschio, M. Rérat, S. Casassa, J. Baima, S. Salustro, B. Kirtman, Quantum-mechanical condensed matter simulations with CRYSTAL, Wiley Interdiscip Rev. Comput. Mol. Sci. 8 (2018) e1360.
[35] A.D. Becke, Density-functional thermochemistry. IV. A new dynamical correlation functional and implications for exact-exchange mixing, J Chem Phys. 104 (1998) 1040. 10.1063/1.470829.
[36] S. Grimme, Semiempirical GGA-type density functional constructed with a long-range dispersion correction, J. Comput. Chem. 27 (2006) 1787–1799, https://doi.org/10.1002/JCC.20495.
[37] P.B.C.S.M.R.R.D. G Sophia, Systematic influence of atomic substitution on the phase diagram of ABO3 ferroelectric perovskites, (2014).
[38] J. Baima, A. Erba, M. Rérat, R. Orlando, R. Dovesi, Beryllium oxide nanotubes and their connection to the flat monolayer, J. Phys. Chem. C 117 (2013) 12864–12872, https://doi.org/10.1021/JP402340Z.
[39] E.O. Gomes, G.S.L. Fabris, M.M. Ferrer, F. v. Motta, M.R.D. Bomio, J. Andres, E. Longo, J.R. Sambrano, Computational procedure to an accurate DFT simulation to solid state systems, Comput Mater Sci. 170 (2019) 109176. 10.1016/j.commatsci.2019.109176.
[40] W.H. Baur, A.A. Khan, IUCr, Rutile-type compounds. IV. SiO2, GeO2 and a comparison with other rutile-type structures, Urn:Issn:0567-7408. 27 (1971) 2133–2139. 10.1107/S0567740871005466.
[41] S. Chae, J. Lee, K.A. Mengle, J.T. Heron, E. Kioupakis, Rutile GeO2: an ultrawide-band-gap semiconductor with ambipolar doping, Appl. Phys. Lett. 114 (2019), 102104, https://doi.org/10.1063/1.5088370.
[42] D.E.P. Vanpoucke, P. Bultinck, I. van Driessche, Extending Hirshfeld-I to bulk and periodic materials, J. Comput. Chem. 34 (2013) 405–417, https://doi.org/10.1002/JCC.23088.
[43] R.M. Hazen, L.W. Finger, Bulk moduli and high-pressure crystal structures of rutile-type compounds, J. Phys. Chem. Solids 42 (1981) 143–151, https://doi.org/10.1016/0022-3697(81)90074-3.
[44] A.A. Bolzan, C. Fong, B.J. Kennedy, C.J. Howard, Structural Studies of Rutile-Type Metal Dioxides, Urn:Issn:0108–7681. 53 (1997) 373–380, https://doi.org/10.1107/S0108768197001468.
[45] M. Stapelbroek, B.D. Evans, Exciton structure in the u.v.-absorption edge of tetragonal GeO2, Solid State Commun. 25 (1978) 959–962, https://doi.org/10.1016/0038-1098(78)90311-3.
[46] K. Robinson, G. v. Gibbs, P.H. Ribbe, Quadratic Elongation: A Quantitative Measure of Distortion in Coordination Polyhedra, Science (1979). 172 (1971) 567–570. 10.1126/SCIENCE.172.3983.567.
[47] R. Hoppe, S. Voigt, H. Glaum, J. Kissel, H.P. Müller, K. Bernet, A new route to charge distributions in ionic solids, J. Less Common Metals. 156 (1989) 105–122, https://doi.org/10.1016/0022-5088(89)90411-6.
[48] G. Deng, Y. Huang, Z. Chen, K. Saito, T. Tanaka, M. Arita, Q. Guo, Heteroepitaxy of (1 0 0)-oriented rutile GeO2 film on c-plane sapphire by pulsed laser deposition, Mater. Lett. 326 (2022), 132945, https://doi.org/10.1016/J.MATLET.2022.132945.
[49] V.L. Deringer, A.L. Tchougréeff, R. Dronskowski, Crystal orbital Hamilton population (COHP) analysis as projected from plane-wave basis sets, J. Phys. Chem. A 115 (2011) 5461–5466, https://doi.org/10.1021/JP202489S/ASSET/IMAGES/LARGE/JP-2011-02489S_0002.JPEG.
[50] K. Momma, F. Izumi, VESTA: a three-dimensional visualization system for electronic and structural analysis, Urn:Issn:0021–8898. 41 (2008) 653–658, https://doi.org/10.1107/S0021889808012016.
[51] J.A.S. Laranjeira, G.S.L. Fabris, M.M. Ferrer, A.R. Albuquerque, J.R. Sambrano, Morphological Transformation Network of Nanoparticles via DFT Simulations, Cryst. Growth Des. 20 (2020) 4600–4611, https://doi.org/10.1021/acs.cgd.0c00423.
[52] J.A.S. Laranjeira, G.S.L. Fabris, A.R. Albuquerque, M.M. Ferrer, J.R. Sambrano, Morphological transformations mapping of CaXO4 (X = Mo or W) and their surface stability, Mater Today Commun. (2022) 104178. 10.1016/J.MTCOMM.2022.104178.
[53] W.J. Li, E.W. Shi, W.Z. Zhong, Z.W. Yin, Growth mechanism and growth habit of oxide crystals, J. Cryst. Growth. 203 (1999) 186–196, https://doi.org/10.1016/S0022-0248(99)00076-7.
[54] C. Jing, W. Sun, W. Wang, Y. Li, J. Chu, Morphology and crystal phase evolution of GeO2 in liquid phase deposition process, J. Cryst. Growth. 338 (2012) 195–200, https://doi.org/10.1016/J.JCRYSGRO.2011.11.024.
[55] M.C. Toroker, D.K. Kanan, N. Alidoust, L.Y. Isseroff, P. Liao, E.A. Carter, First principles scheme to evaluate band edge positions in potential transition metal oxide photocatalysts and photoelectrodes, PCCP 13 (2011) 16644–16654, https://doi.org/10.1039/C1CP22128K.